Energy Storage Materials 52 (2022) 291–298

Contents lists available at ScienceDirect

Energy Storage Materials

journal homepage: www.elsevier.com/locate/ensm

Revealing excess Al^{3+} preinsertion on altering diffusion paths of aluminum vanadate for zinc-ion batteries

Lingli Xing [a,b], Chengyi Zhang [c], Ming Li [a], Ping Hu [a], Xinyu Zhang [a], Yuhang Dai [a], Xuelei Pan [a], Weiyi Sun [a], Shanlin Li [b], Junmin Xue [b], Qinyou An [a,d,*], Liqiang Mai [a,d,*]

[a] State Key Laboratory of Advanced Technology for Materials Synthesis and Processing, Wuhan University of Technology, Wuhan 430070, PR China
[b] Department of Materials Science and Engineering, National University of Singapore, 117575, Singapore
[c] Institute of Technological Sciences, Wuhan University, Wuhan 430072, PR China
[d] Foshan Xianhu Laboratory of the Advanced Energy Science and Technology Guangdong Laboratory, Xianhu hydrogen Valley, Foshan 528200, PR China

ARTICLE INFO

Keywords:
Aqueous zinc-ion batteries
$H_{11}Al_2V_6O_{23.2}$
Excessive ion intercalation
Diffusion path
Reaction mechanism

ABSTRACT

Layered metal vanadates have been extensively investigated for aqueous zinc-ion batteries (AZIBs) due to their low cost, crystal structure, and a wide diversity of vanadium valence states. However, research on the number of cationic pre-intercalation layers is almost empty and the effect of Al atomic numbers in $H_{11}Al_2V_6O_{23.2}$ (HAVO) on the diffusion path has not been studied even more. The systematic investigation into pre-intercalated ions in electrode materials is fundamental but vital for the further development of high-performance batteries of both the point of academic and industry. In this contribution, we designed and synthesized HAVO with four different layer spacings by simply modulating aluminum content for the first time and combined a range of *ex-situ* and *in-situ* complementary techniques to reveal the reaction mechanism of zinc ion storage and its intrinsic relationship with electrochemical performance. The "pillar" effects of stable Al^{3+} between the interlayers protects the laminate structures from collapse during electrochemical process and effectively widens the layer spacing at the same time. However, based on experiments and calculations we have demonstrated that the appropriate aluminum content can significantly improve the electrochemical properties of the material, while excessive ion intercalation can block the zinc ions diffusion channels. As a result, HAVO with a suitable Al atomic number displays extraordinary electrochemical performance. This work provides further insights into the design and construction of cathodes for pre-inserted ion batteries, and facilitates the exploitation of low-cost and high-safety cathodes.

1. Introduction

Rechargeable aqueous zinc-ion batteries (AZIBs) are very prospective in exploring alternative rechargeable storage devices to lithium-ion due to emerging, economic and practical factors [1–4]. Rechargeable AZIBs have gained widespread interest due to the distinctive virtues of Zn, comprising highly theoretical capacity (820 mA h g^{-1} and 5855 mA h cm^{-3}), lower redox potential (−0.76 V versus typical hydrogen electrodes), environmental safety, high reliability in water, simplicity of handling, non-toxicity, low cost, and abundance of resources [5–8]. These merits make the exploitation of the AZIBs a global priority and offer a prospective candidature for massive electrical energy storage. Yet, the rate capability, specific capacity, and cycling stability are limited by the cathode material [9,10]. The quest for cathode materials with a stable structure is thus imperative but the central theme to be addressed.

Over the last decades, there has been a growing trend of concern for Vanadium based compounds, notably vanadium oxides, as cathode candidates for progressing secondary batteries, given their reduced cost, varying crystal structure, and wide diversity of vanadium valence states [6,11–14]. Since hundreds of V-based types of materials with different layers or tunnel spacings have been identified, they are highly suitable as preferred candidates. Further researches into vanadium-based cathode materials for ZIBs have been prompted by recent advances in VO_2 [15], V_2O_5 [16], $V_2O_5{\cdot}nH_2O$ [17], $VOPO_4{\cdot}2H_2O$ [18], $Ca_{0.25}V_2O_5{\cdot}nH_2O$ [19], $K_2V_8O_{21}$ [20], $Na_2V_6O_{16}{\cdot}1{\cdot}63H_2O$ [2], $(NH_4)_2V_3O_8$ [21], $NH_4V_4O_{10}$ [22], and VS_2 [23].

Even though considerable efforts have been made with vanadium-

* Corresponding authors.
E-mail addresses: anqinyou86@whut.edu.cn (Q. An), mlq518@whut.edu.cn (L. Mai).

https://doi.org/10.1016/j.ensm.2022.07.044
Received 22 May 2022; Received in revised form 24 July 2022; Accepted 30 July 2022
Available online 30 July 2022
2405-8297/© 2022 Elsevier B.V. All rights reserved.

based materials for AZIBs, the rational design is still in the infancy and further research is necessary to upgrade all facets of their performance. Early studies have revealed that decreasing particle size and modifying the morphology of electrode materials can remarkably enhance their cycling stability and rate capability in AZIBs and other battery systems [24]. The ion pre-intercalation strategy is an effective method of increasing diffusion channels, facilitating the intercalation of zinc ions and improving electrochemical kinetics and rate performance. Aluminum is the most metal-rich element in the Earth's crust (8.3% of the surface) and has the advantage of being less costly (~1.4 USD kg^{-1}) and less toxic than transition metals [12]. In addition, trivalent Al^{3+} forms stable Al-O bonds between O atoms with a lattice energy of 15, 111 kJ mol^{-1}, significantly higher than Na-O (2478 kJ mol^{-1}), K-O (2232 kJ mol^{-1}), and Ca-O (3401 kJ mol^{-1}) [25]. Contrary to transition metal ions, the empty d orbitals and stabilized value state of Al 3p reduce Coulombic interactions with the guest ion during cycling. During repeated insertion/extraction of Zn^{2+}, the structure of V_2O_5 tends to collapse, leading to a rapid decay of its capacity, and therefore stabilization is more pronounced when Al^{3+} is pre-inserted into V_2O_5. The introduction to metal ions has become the main strategy to solve this problem, which involves an increase in the layer spacing. Nevertheless, the altering of hydrogen aluminum vanadium oxide interlayer spacing using Al ions has rarely been investigated, and studying the impact on aluminum content of HAVOs on the performance of AZIBs has never been explored, and the mechanism of zinc storage in HAVO is unclear.

To explore the effect of the number of cationic pre-inserted layers on the electrochemical performance of vanadium oxides, we prepared HAVOs with different numbers of pre-inserted Al^{3+} and tested their cycling and rate behavior, using a common layered vanadium oxide as a model for aluminum insertion. In this contribution, we designed and constructed HAVOs with different sizes, morphologies, and (001) crystal plane lattice spacings using a simple hydrothermal synthesis method by adjusting the aluminum content for the first time. The inclusion of Al^{3+} provides enhanced structural stability and electronic conductivity of the samples. And on the basis of experimental analysis and theoretical calculations, the effect of different aluminum content on its zinc storage performance was systematically studied. The HAVO prepared with suitable aluminum content presented excellent electrochemical properties, consisting of a significantly larger specific capacity (416.3 mA h g^{-1} at 300 mA g^{-1}), better rate performance (138.9 mA h g^{-1} at 5000 mA g^{-1}) and greater cycling stability (148.1 mA h g^{-1} capacity remaining after 10,000 cycles at 3000 mA g^{-1}) than other aluminum content HAVOs. Furthermore, a series of *ex-situ* and *in-situ* complementary techniques such as X-ray diffraction (XRD), Raman spectra, Fourier transform infrared (FTIR) for *in-situ* characterization and X-ray photoelectron spectroscopy (XPS), high-resolution transmission electron microscopy (HRTEM) for *ex-situ* characterization and *in-situ* electrochemical impedance spectroscopy (EIS) were adopted to reveal the mechanism of Zn^{2+} storage.

2. Results and discussion

Based on the inductively coupled plasma (ICP) results (Table S1), the Al content increases sequentially, which is consistent with the aluminum source ratio increasing during synthesis. The as-prepared HAVOs with different aluminum contents, named HAVO-10.1, HAVO-11.0, HAVO-11.3, and HAVO-12.5 according to the Al atomic number. The crystal structures of HAVO-10.1, HAVO-11.0, HAVO-11.3, and HAVO-12.5 are first shown, as presented in Fig. 1a. All the peaks of the plots are well-matched with the phase of $H_{11}Al_2V_6O_{23.2}$ monoclinic crystal structure (Lattice parameters: a = 11.14 Å, b = 3.62 Å, c = 13.29 Å, α=90.0, β=90.7, γ=90.0, JCPDS card no. 49–0693). The strong peaks at 7.00°,

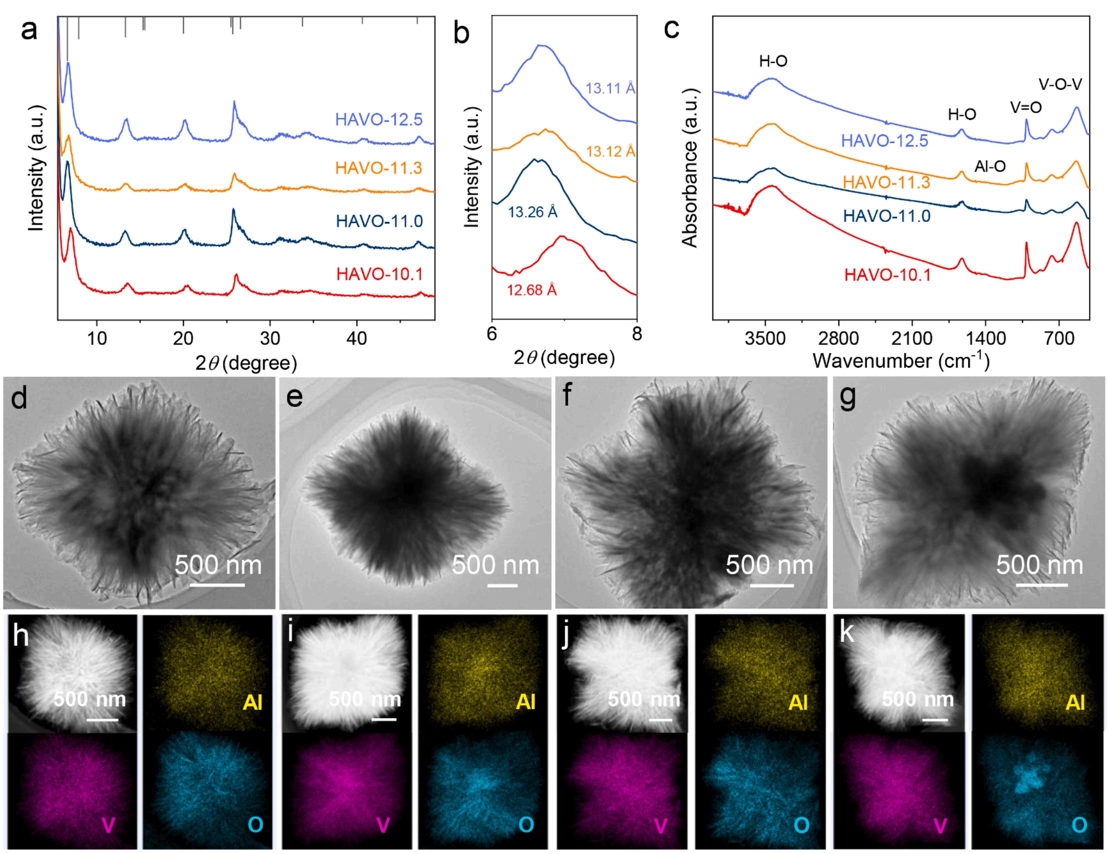

Fig. 1. (a) Powder XRD patterns, (b) enlargement of selected regions, and (c) FTIR spectra of HAVOs. (d) TEM image of HAVO-10.1, (h) HAADF-STEM image and corresponding Al, V, O element mapping. (e) TEM image of HAVO-11.0, (i) HAADF-STEM image and EDS mapping image. (f) TEM image, (j) HAADF-STEM image and EDS mapping image of HAVO-11.3. (g) TEM image of HAVO-12.5, (k) HAADF-STEM image and EDS mapping image.

6.60°, 6.68°, and 6.72° of HAVOs in Fig. 1b correspond to the (001) crystal plane with lattice spacings calculated from Bragg's law of 12.68 Å, 13.26 Å, 13.12 Å, and 13.11 Å. This is approximately three times larger than pristine V_2O_5 (4.4 Å, JCPDS no. 41–1426) than any other previously reported vanadium-based cathodes [26,27]. Large interlayer spacing of the (001) plane is achieved by the addition of Al^{3+} to the layered structure of vanadium oxide [28–30]. In the Raman spectra (Figure S1), HAVOs exhibit a comparable spectrum to that of V_2O_5 [31]. Figure S2 shows a partial Raman fit of HAVO-11.0, where the fitted peak at 644 cm^{-1} corresponds to an Al-O bond, indicating the formation of a strong chemical bond between the Al and O atoms rather than a weak interaction [32,33].

Thermogravimetric analysis (TGA) curves (Figure S3) were employed to investigate the water content of HAVOs. The weight of HAVOs continued to decrease with increasing temperature until it arrived at approximately 400 °C, after which it remained almost constant. The weight losses between room temperature and 400 °C for HAVO-10.1, HAVO-11.0, HAVO-11.3, and HAVO-12.5 were 19.8%, 11.4%, 11.6% and 12.2%. The water content in HAVO-10.1 was higher than in the other three HAVOs. The presence of the Al-O bonds is evidenced by the 1402 cm^{-1} peak in the FTIR spectra of HAVOs (Fig. 1c) [34]. The other peaks are similar to those found in the FTIR spectrum of $V_2O_5{\cdot}nH_2O$, with peaks at 1003, 762, and 527 cm^{-1} allocated to symmetric stretching vibrations of $V = O$, and asymmetric and symmetric stretching vibrations of V-O-V [35,36]. The broad peak at 3421 cm^{-1} and peak at 1623 cm^{-1} confirm the presence of interlayer water molecules. Figure S4 shows the nitrogen adsorption-desorption isotherms for HAVOs. The Brunauer-Emmett-Teller (BET) surface areas for HAVO-10.1, HAVO-11.0, HAVO-11.3, and HAVO-12.5 are 209, 365, 270, and 227 $m^2\ g^{-1}$ respectively. From the pore size distribution curves (Figure S5), the average mesoporous pore sizes of HAVO-10.1, HAVO-11.0, HAVO-11.3, and HAVO-12.5 for desorption were 8.45 nm, 6.35 nm, 7.09 nm, and 7.96 nm, respectively.

Scanning electron microscopy (SEM) (Figure S6) and transmission electron microscopy (TEM) (Fig. 1d-g) images show that these obtained HAVOs have a relatively homogeneous and refined morphology. In addition, the XPS spectrum was used to determine the bonding structure of HAVOs. The full XPS spectra (Figure S7) shows the characteristic bands of Al, C, V, and O in HAVOs. The ratio of Al 2p in HAVO-10.1, HAVO-11.0, HAVO-11.3, and HAVO-12.5 was determined to be 1:9.45:18.96:28.06 by assessing the integrated area in the spectra. The area of Al 2p increases as the number of Al atoms increases. Figure S8 exhibits the high-resolution V 2p spectra of HAVOs, for HAVO-11.0 the peaks at 517.7 and 525.1 eV respond to $2p_{3/2}$ and $2p_{1/2}$ of V^{5+}. In the addition, the V^{4+} peaks at 516.1, and 523.9 eV indicate the production of the lower valence state of V. The presence of mixed valence

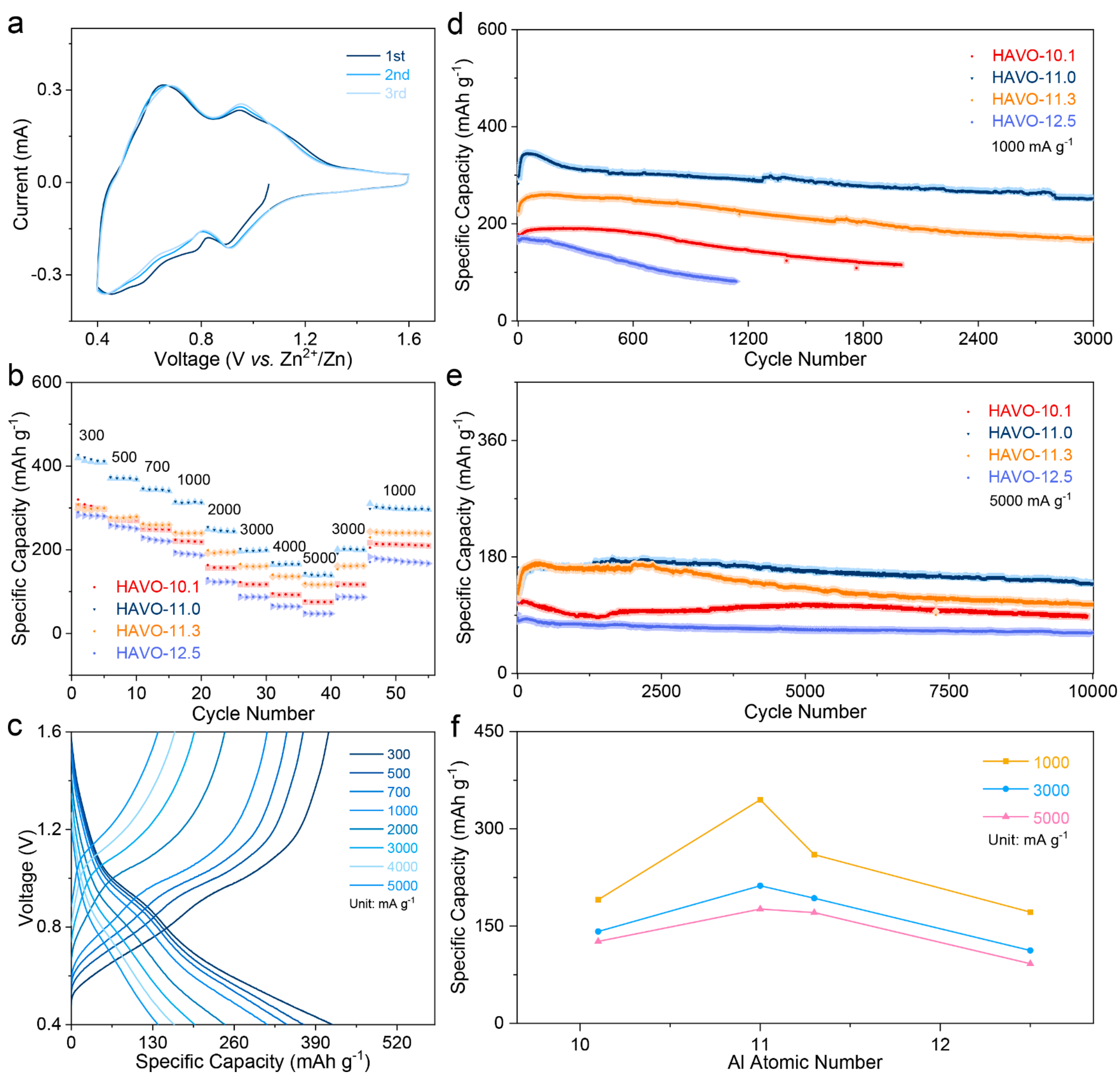

Fig. 2. (a) The first three CV curves of HAVO-11.0. (b) Rate capabilities of HAVOs. (c) Charge-discharge curves of HAVO-11.0. Cycling performances tested of HAVOs at (d) 1000 and (e) 5000 mA g^{-1}. (f) A comparison of the capacitive contribution at different Al atomic numbers of HAVOs.

states in HAVO-11.0 can effectively enhance the intrinsic electronic conductivity [37]. Fig. S9 presents the high-resolution O 1 s spectra of HAVOs, and for HAVO-11.0 the resolving peaks of the O 1 s spectra can be analyzed down to 530.3, 531.5, and 532.9 eV. The band at 530.3 eV is owing to O^{2-} bound to vanadium, the peak at 531.5 eV is due to OH^-, and the small peak at 532.9 eV is attributed to crystal water [6,38].

First, cyclic voltammetry (CV) measurements were performed on HAVO-11.0 at 0.2 mV s^{-1} over a potential range of 0.4 to 1.6 V in AZIBs (Fig. 2a). The first three CV curves of HAVO-11.0 were similar, with three pairs of redox peaks observed. In detail, two pairs of relatively distinct reversible redox peaks correspond to the changes in oxidation-state of V from V^{5+} to V^{4+} (0.95/0.91 V) and V^{4+} to V^{3+} (0.67/0.69 V), demonstrating a multistep (de)intercalation of Zn^{2+}, which is common in other vanadium-based cathodes [17,28]. The voltage plateaus in the first three charge/discharge curves agree well with the redox peaks in the CV curve (Figure S10). In a comparison of the rate performance shown in Fig. 2b, HAVO-11.0 came out on top of the four samples with reversible discharge specific capacities of 416.3, 371.3, 344.3, 312.8, 245.6, 197.5, 165.6, and 138.9 mA h g^{-1} at 300, 500, 700, 1000, 2000, 3000, 4000, and 5000 mA g^{-1}, respectively. When returning to 1000 mA g^{-1}, the discharge specific capacity is 301.4 mA h g^{-1}. The corresponding rate performance of the discharge/charge curves implicate ultra-fast Zn^{2+} storage and low polarization of HAVO-11.0 (Fig. 2c). When tested at 300 mA g^{-1}, HAVO-11.0 has an even higher reversible discharge specific capacity of 416.3 mA h g^{-1} than HAVO-10.1, HAVO-11.3, and HAVO-12.5 (304.9, 297.9, and 282.3 mA h g^{-1}).

In particular, the HAVO-11.0 electrode also revealed excellent long cycle stability, retaining a specific capacity for 252.9 mA h g^{-1} even after 3000 cycles at 1000 mA g^{-1} (Figs. 2d and S11). In contrast, the HAVO-12.5 electrode showed rapid capacity decay, from 171.7 mA h g^{-1} to 82.8 mA h g^{-1} after 1100 cycles. In meantime, the cycling performance of HAVOs were also studied at 3000 (Figure S12) and 5000 mA g^{-1} (Fig. 2e). In particular, for HAVO-11.0, high reversible specific capacities of 148.1 and 138.9 mA h g^{-1} are maintained after 10,000 cycles at 3000 and 5000 mA g^{-1} (Figure S13 and S14), confirming its outstanding long-term cycling stability under typical battery operating conditions. As shown in Figures S15–17, the other three HAVOs exhibit more pronounced capacity decay after a long cycle. The capacitive contribution of HAVOs at different Al atomic numbers is summarized in Fig. 2f. HAVO-11.0 shows rapid Zn^{2+} storage and excellent long-term cycling stability, which is mostly ascribed to the interlayer structure with suitable aluminum ion concentration [39,40]. The large capacity, long-cycling stability and superior rate performance of HAVO-11.0 demonstrate that HAVO-11.0 is a promising candidate cathode for AZIBs.

In addition, to achieve a better understanding of the underlying reasons behind the excellent cyclability with good rate performance of HAVO-11.0, CV curves Fig. 3a) were measured for different sweep rates and a detailed kinetic analysis was carried out. In previous reports, the correlation of current (i) and scan rate (v) was presented by formula ((1) [41]:

$$i = av^b \tag{1}$$

The b value can represent the rate-limiting step in the process of electrochemistry and therefore the charging storage mechanism. The equation is transformed so that the value of b is strongly reliant on the value of the slope of the log(i)-log(v) plot (Fig. 3b). The b values for the a and a' peaks of HAVO-11.0 were evaluated as 0.98 and 0.86 for scan

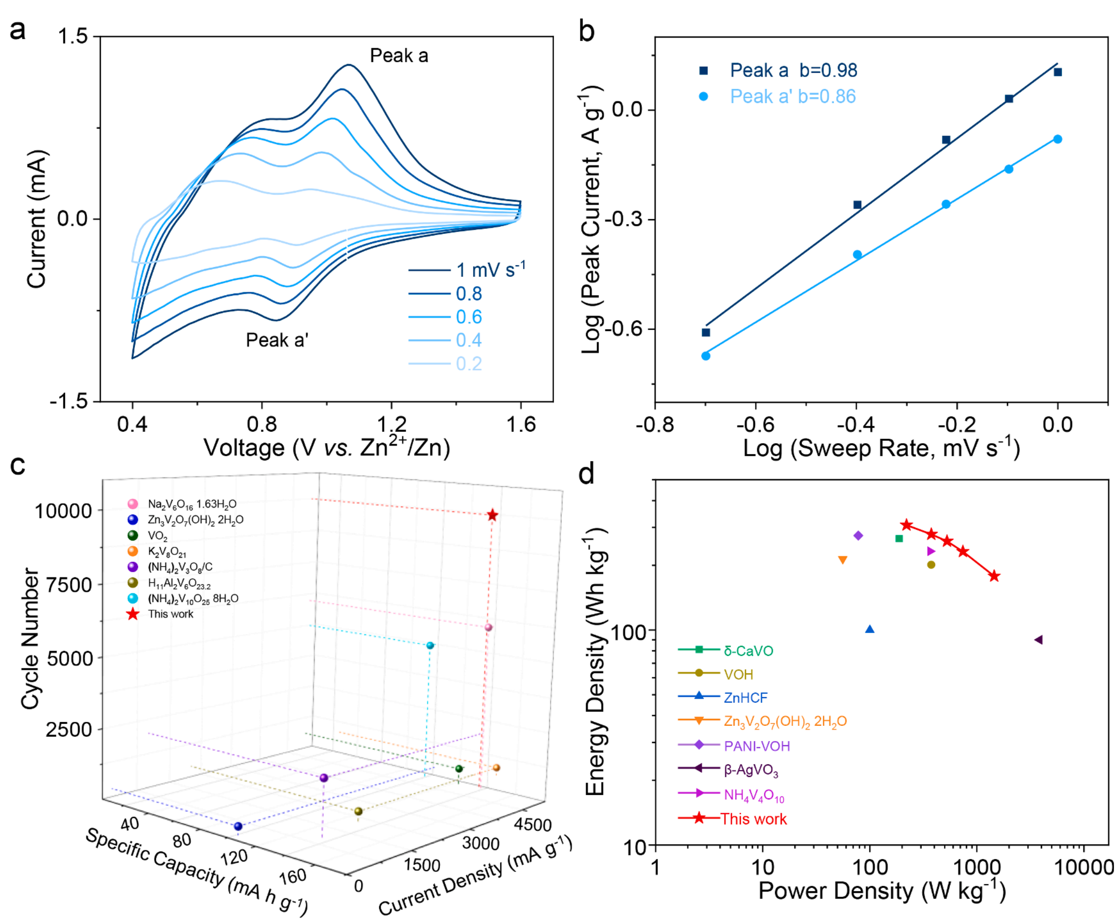

Fig. 3. (a) CV curves of HAVO-11.0 at different scan rates. (b) The plots of log (peak current) versus log (sweep rate) at each peak from CV curves of HAVO-11.0. (c) Comparison of cycling performance with other V-based cathodes. (d) Ragone plots of HAVO-11.0 and other representative cathode materials for AZIBs.

rates from 0.2 to 1.0 mV s^{-1}. Values of b of 0.5 denote diffusion-controlled process, whereas b values of 1.0 indicate surface-controlled processes. This phenomenon suggests that HAVO-11.0 has an ultra-fast and surface-controlled kinetics with typical capacitive properties. The CV curves and corresponding log(i)-log(v) curves for other HAVO samples are presented in Figures S18, S19, and S20.

Benefitting from the correct metal ion concentration-dependent properties described above, it is evident that the rate-capacity of HAVO-11.0 exceeds that of most previously reported V-based cathodes, including $Na_2V_6O_{16}\cdot 1{\cdot}63H_2O$ [2], $Zn_3V_2O_7(OH)_2\cdot 2H_2O$[14], VO_2 [15], $K_2V_8O_{21}$ [20], $(NH_4)_2V_{10}O_{25}\cdot 8H_2O$[27], $H_{11}Al_2V_6O_{23.2}$ [30], and $(NH_4)_2V_3O_8/C$ [21], illustrating the significance and importance of this work (Fig. 3c). Subsequently, the HAVO-11.0 achieves a high energy density of 307.4 W h kg^{-1} at a power density of 220.1 W kg^{-1} owing of its high specific capacity and voltage platform, which compares favourably with many reported cathode materials such as δ-CaVO [42], VOH [43], ZnHCF [44], $Zn_3V_2O_7(OH)_2\cdot 2H_2O$ [14], PANI-VOH [45], β-$AgVO_3$ [46], and $NH_4V_4O_{10}$[47] (Fig. 3d) with a clear advantage.

To study the zinc ion storage mechanism of the HAVO-11.0 cathode, we performed *ex-situ* (Fig. 4a) and *in-situ* (Fig. 4b) XRD experiments on the HAVO-11.0 cathode. The *ex-situ* XRD experiments we carried out at different charge-discharge states to investigate its structural evolution. Apparently in the range of 10° to 80°, the characteristic peaks of HAVO-11.0 were not significantly shifted at different states and no new diffraction peaks were detected, only changes in peak intensity (more pronounced in Fig. 4b), indicating a well-preserved lamellar structure. The peaks intensity varied regularly as charging and discharging progressed. A phase shift in HAVO-11.0 was found by detailed observation of the (001) peak before 10° During the discharge, the (001) peak shifts slightly to a higher 2θ position when the Zn^{2+} ions are inserted and the interlayer distance is contracted. This contraction is attributed to the insertion of the Zn^{2+} into HAVO-11.0 when its water molecules come off. As charging proceeds, the (001) peak is shifted towards the lower 2θ position and when Zn^{2+} is completely delaminated and the water molecules are re-inserted, the XRD pattern of the electrode is quite comparable to that of the pristine electrode. This demonstrates that the (de) intercalation of Zn^{2+} in HAVO-11.0 is highly reversible and confirms the Zn^{2+} intercalation reaction mechanism. Water molecules are believed to play a crucial role in this process, including a buffer to the high charge density of Zn^{2+}, a reduction in the activation energy of charge transfer, and an alteration of the lamellar corridor to allow Zn^{2+} entry/exit [1, 48].

Fig. 4c shows the *in-situ* FTIR spectra of the HAVO-11.0 electrode in different electrochemical states. Apart from a more pronounced shift of the peak at 3421 cm^{-1} (which belongs to O—H stretching vibration), there is no significant shift of other peaks, indicating that the molecular structure remains unchanged during the electrochemical process [49]. In other words, these inorganic components are very stable during cycling and conducive to long cycle performance. For the second discharge, the peak at 3470 cm^{-1} is clearly observed to be shifted to a higher wavenumber and gradually weakened, while during charging the peak at 3439 cm^{-1} is shifted to a lower wavenumber and gradually intensified, which is consistent with the 001 peak shift during the insertion and extraction of water molecules in *ex-situ* XRD.

Furthermore, *in-situ* Raman spectra have driven further in-depth research into the reaction mechanism of the HAVO-11.0 electrode during the electrochemical process (Fig. 4d). The Raman characteristic peaks at 267, 513, and 700 cm^{-1} originate from V-O-V vibrations, while Raman bands located 95 and 161 cm^{-1} are designated as lattice vibrations [39,40,50]. At the first charge to 1.6 V, the Zn^{2+} ions are removed from the HAVO-11.0 electrode and peaks at 95, 161, 267, 513, and 700 cm^{-1} appear. During the subsequent discharge process, the Zn^{2+} ions are

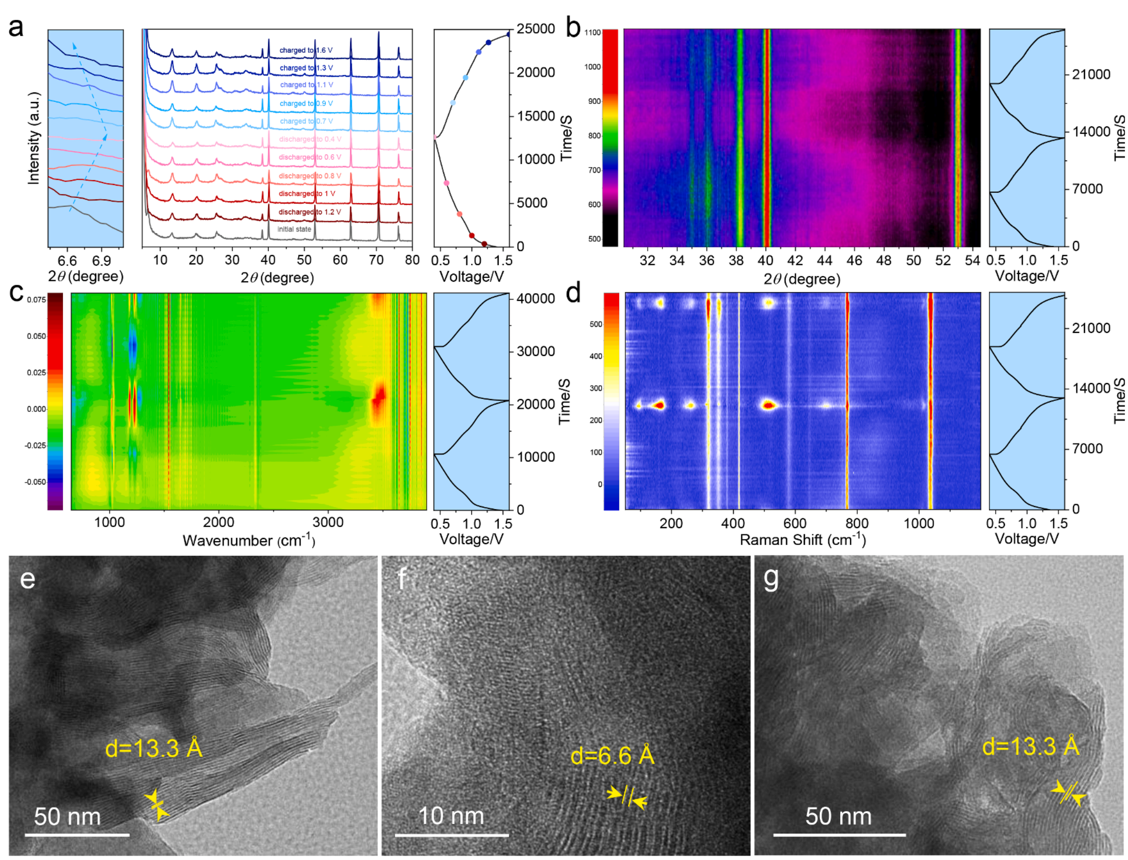

Fig. 4. (a) *Ex-situ* and (b) *in-situ* XRD patterns, (c) *in-situ* FTIR spectra, (d) *in-situ* Raman spectra of HAVO-11.0 electrode. *Ex-situ* HRTEM images of HAVO-11.0 electrode (e) in pristine, (f) fully discharged and (g) charged states.

intercalated in the HAVO-11.0 electrode and these characteristic peaks disappear again and no new peaks are generated. Subsequently, the characteristic peaks appear again until the next charge at 1.6 V. As expected, the regular disappearance or appearance of these characteristic Raman peaks indicates a completely reversible behavior of the electrochemical reaction, which suggests a good reversibility of the Zn^{2+} insertion/extraction. This reversible behavior is also in agreement with the *in-situ* XRD and *in-situ* FTIR results. Additionally, there is no significant shift in the position of these peaks during the different electrochemical processes, only a change in intensity.

To have a further insight into the electrochemical behaviors of the HAVO-11.0, *in-situ* EIS study was carried out as shown in Figure S21 and Figure S22. During first cycle of discharge, when the discharge voltage dropped to around 0.95 V (at the end of the first plateau), the semicircle in the low frequency region changed significantly and the impedance reached its lowest level. As the depth of discharge proceeds a second plateau appears, at which point the impedance gradually increases, evolving in a V-shape, and at the latter period of discharge the curve appears to return to its original state (the uncycled state, black line in Figure S21), but notably not exactly the same. These results show that the charge transfer resistance (R_{ct}) is concerned in the content of Zn^{2+} in the active material, the more Zn^{2+}, the smaller R_{ct} [51]. The trend of the impedance curve is reversed during the charging phase of the first cycle, when charging reaches 1 V (the first plateau appears) and a distinct semicircle appears in the low frequency region, indicating that the voltage plateau is the inflection point for the resistance change of the HAVO-11.0. The R_{ct} of HAVO-11.0 appears gradually during discharge and then increases and disappears during charging.

The electrochemical mechanism of the Zn^{2+} (de)intercalation process of the HAVO-11.0 was investigated using *ex-situ* XPS spectra. No zinc signal could be detected in the XPS spectrum of the pristine HAVO-11.0 electrode (Figure S23), when HAVO-11.0 electrode was discharged, two distinct peaks at 1022.7 and 1045.8 eV appeared for Zn $2p_{3/2}$ and Zn $2p_{1/2}$, meaning the successful insertion of Zn^{2+} into the HAVO-11.0 electrode. Even though not all zinc ions are removed after charging, the residual Zn^{2+} acting as interlayer pillars maintains the stability of the laminate structure. In the *ex-situ* XPS spectra of V 2p in the pristine state (Figure S24), there are four peaks at 517.7, 525.2, 516.4, and 523.3 eV that can be decomposed, corresponding to the dominant V^{5+} and a small fraction of V^{4+}, respectively. Compared to the pristine state, when the HAVO-11.0 electrode is discharged to 0.4 V, there is V^{3+} components at 516.3 and 522.7 eV, while the intensity of V^{4+} (517.7 and 524.3 eV) is significantly enhanced and that of V^{5+} (518.2 and 525.5 eV) is significantly reduced, indicating that during Zn^{2+} intercalation process, the V^{5+} (V^{4+}) is partially reduced to V^{4+} (V^{3+}). When charged to 1.6 V, the V^{5+} and V^{4+} signals to reappear and the intensity and position of the peaks largely return to their initial state. The XPS results confirmed the reversible (de)intercalation of Zn^{2+} during the discharging and charging of HAVO-11.0. For a deeper insight into the reversible Zn^{2+} storage mechanism, *ex-situ* HRTEM measurements were carried out on HAVO-11.0 electrode (Fig. 4e-g). During the discharge process, zinc ions are intercalated and water molecules are deintercalated, leading to a reduction in interlayer distances. During the charging process, zinc ions are taken off and water molecules are intercalated, and the interlayer distance rises back to 13.3 Å (corresponds to the (001) plane), which is the same as the interlayer distance of the pristine electrode.

Based on these results, the whole electrochemical of the Zn/HAVO-11.0 cell could be presented by:

$$Anode:\ Zn \leftrightarrow Zn^{2+} + 2e^-$$

$$Cathode:\ H_{11}Al_2V_6O_{23.2} + xZn^{2+} + 2xe^- \leftrightarrow Zn_xH_{11}Al_2V_6O_{23.2}$$

In addition, to gain insight into the kinetics of Zn^{2+} diffusion in the HAVO-11.0 electrode, galvanostatic intermittent titration technique (GITT) was performed to analyze chemical diffusion coefficient of Zn^{2+} during discharge, and the GITT curves are shown in Figure S25. The D_{Zn} can be obtained from the following formula (2) [52]:

$$D = \frac{4}{\pi\tau}\left(\frac{m_B V_M}{M_B S}\right)^2 \left(\frac{\Delta E_S}{\Delta E_\tau}\right)^2 \tag{2}$$

where τ, m_B, V_M, M_B, and S are the constant current pulse time, the mass, the molar volume of the material, the molecular weight and the electrode/electrolyte contact area, respectively. ΔE_S is the voltage difference during the open circuit and ΔE_τ is the total change in cell voltage during the constant current pulse. The Zn^{2+} diffusion coefficient of HAVO-11.0 was calculated to be 10^{-10} to 10^{-9} $cm^2\ s^{-1}$. This result suggests that HAVO-11.0 allows for rapid Zn^{2+} migration, leading to long-period stability and excellent rate performance.

The experimental observation is fully confirmed by the density functional theory (DFT) calculations (The detailed calculation method is presented in the supporting information). The mole ratios of the Al to V of the samples HAVO-10.1, HAVO-11.0, HAVO-11.3, and HAVO-12.5 are 0.1670, 0.1818, 0.1867, and 0.2078 (10.1, 11.0, 11.3, and 12.5 Al ions in the bulk structure) individually. To adequately match the experiment, we investigate the microstructural evolution and behavior of Zn in the HAVO where the number of Al ions from 9 to 13 in the bulk.

As presented in Fig. 5a, with the insertion of Al^{3+}, the layer spacing of VO shows a trend of first increasing and then decreasing. Among them, the layer spacing reaches the maximum when 11 aluminum ions are intercalated. At this time, the insertion and the desertion of the Zn^{2+} will be the smoothest and cause the least damage towards the structure, which effectively ensures the long cycling stability. The transport rate of the Zn^{2+} in the cathode is also the major factor affecting the overall performance of the batteries. To deeply understand the migration behavior of the Zn^{2+} in the cathode, we also take a series of calculations. Two migration paths, path-A and path-B, have been colorfully demonstrated in Fig. 5b. When the doping number of Al^{3+} approach 11, the Zn^{2+} migrate along Path-A. With the insertion of Al^{3+}, the larger layer spacing makes the migration of Zn^{2+} smoother. However, when the number of intercalated Al^{3+} reaches 12, Path A is completely blocked and Zn^{2+} can only migrate through Path-B (Fig. 5c). At this point, the migration barrier becomes instantly larger (Fig. 5d). The results of the first-principles simulations are in full agreement with the long-cycle results measured in the experiments. Our experiments and calculations fully validate that the pre-insertion ions can act as a pillar to expand the layer spacing and improve the stability of the structure during the long-cycling test. However, too many pre-inserted ions will not only occupy the Zn^{2+} insertion sites and then reduce the capacity of the material, but will also block the zinc ion transport channels and reduce the rate performance of the material.

3. Conclusion

In summary, we purposefully constructed HAVOs with different Al atomic numbers for the first time by a one-step hydrothermal method, and systematically investigated the effect of different Al atomic numbers on its zinc storage performance and revealed the zinc storage mechanism. The obtained electrochemical performance of HAVO-11.0 is considerably enhanced, mainly due to the short electron/ion transport length, high electron conductivity, wide specific surface area, and structural stability, along with improved charge transfer properties and ion diffusion kinetics with the help of crystal water. The HAVO-11.0 delivers a high specific capacity (416.3 mA h g^{-1} at 300 mA g^{-1}), excellent cycling stability (148.1 mA h g^{-1} capacity remaining after 10,000 cycles at 3000 mA g^{-1}) and outstanding rate capability (138.9 mA h g^{-1} at 5000 mA g^{-1}) when used in AZIBs. Furthermore, based on crystal structure analysis, electrochemical tests and DFT calculations, we conclude that proper insertion of Al^{3+} into the permissive structure can effectively widen the layer spacing and thus surmount the cycling and rate limitations of HAVOs, but not in greater amounts, as excess Al^{3+} can block the diffusion channels of zinc ions, altering the diffusion path

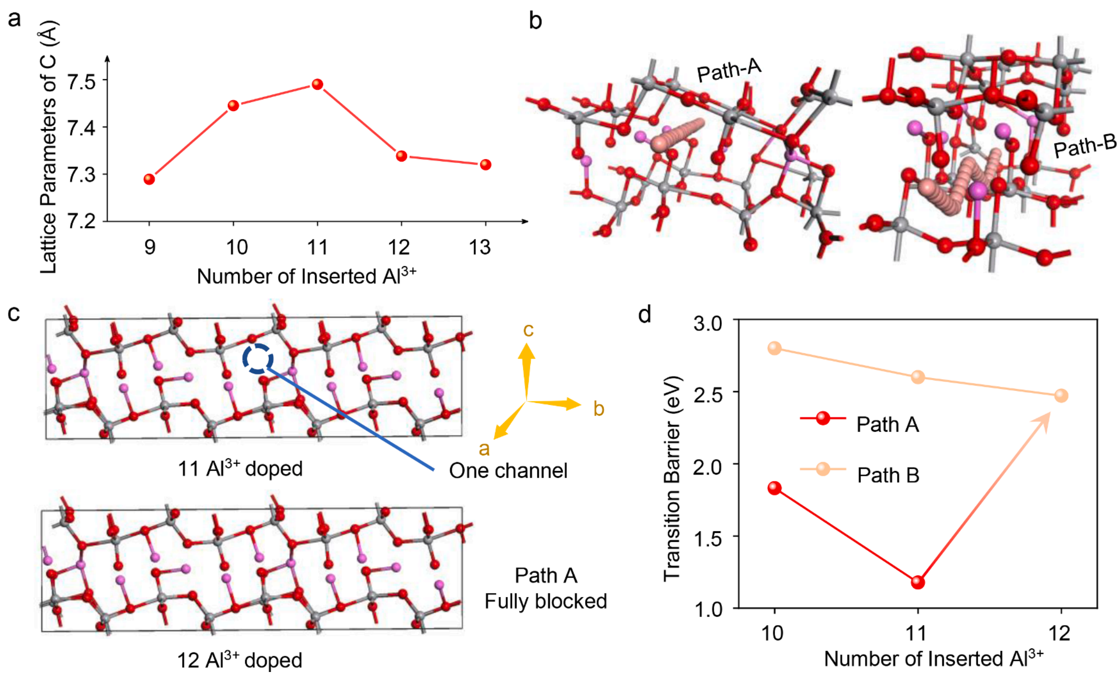

Fig. 5. (a) Relationship between the amount of Al^{3+} and the lattice parameter of c. (b, c) Sketch map of the two migration paths of Zn^{2+} in the cathode. (d) Migration barrier of the Zn^{2+} in two paths individually.

and thus reducing the rate performance. These findings may provide some inspiration for researchers in designing and exploring more promising cathode materials for AZIBs for more advanced energy-related applications.

4. Experimental section

4.1. Fabrication of HAVOs

A rapid and adjustable hydrothermal method was used to synthesis highly homogeneous HAVOs. First, NH_4VO_3 (468 mg) was dispersed in deionized (DI) water with Pluronic® F127 (468 mg) under magnetic stirring at 60 °C and hydrochloric acid was added until the solution pH=2.5. Then, a certain amount of $AlCl_3$ (533 mg $AlCl_3$ corresponding to HAVO-10.1, 800 mg $AlCl_3$ to HAVO-11.0, 1334 mg $AlCl_3$ to HAVO-11.3 and 2134 mg $AlCl_3$ to HAVO-12.5) were added to the above solution and transferred to an autoclave for 10 h at 160 °C. After centrifugation, washing with DI water and ethanol and drying, HAVOs are obtained.

4.2. Electrochemical characterization

CR2016 coin cells were assembled by sandwiching a Grade GF/D Whatman glass microfiber filter filled with the electrolyte ($Zn(CF_3SO_3)_2$ aqueous solution) between the prepared cathode and the zinc foil anode. The working electrode was composed of 70 wt% active material, 20 wt% acetylene black and 10 wt% polyvinylidene fluoride (PVDF). Galvanostatic discharge/charge tests were performed using a Neware battery test system (CT-4008T-5V10mA-164, Shenzhen China). Galvanostatic intermittent titration technique (GITT) curve was recorded at a multi-channel battery testing system (LAND CT2001A). Electrochemical impedance spectroscopy (EIS) and cyclic voltammetry (CV) measurements were conducted with an Auto lab PGSTAT302 N.

Declaration of Competing Interest

The authors declare that they have no known competing financial interests or personal relationships that could have appeared to influence the work reported in this paper.

Data Availability

Data will be made available on request.

Acknowledgements

L. X. and C. Z. contributed equally to this work. This work was supported by the National Key Research and Development Program of China (2020YFA0715000), the National Natural Science Foundation of China (51832004, 52127816, 52172231, 51972259), and Foshan Xianhu Laboratory of the Advanced Energy Science and Technology Guangdong Laboratory (XHT2020–003). Support from the China Scholarship Council (CSC).

Supplementary materials

Supplementary material associated with this article can be found, in the online version, at doi:10.1016/j.ensm.2022.07.044.

References

[1] M. Song, H. Tan, D. Chao, H. Fan, Recent Advances in Zn-Ion Batteries, Adv. Funct. Mater. 28 (2018), 1802564.
[2] P. Hu, T. Zhu, X. Wang, X. Wei, M. Yan, J. Li, W. Luo, W. Yang, W. Zhang, L. Zhou, Z. Zhou, L. Mai, Highly Durable $Na_2V_6O_{16}\cdot1.63H_2O$ Nanowire Cathode for Aqueous Zinc-Ion Battery, Nano Lett. 18 (2018) 1758–1763.
[3] F. Wan, Z. Niu, Design Strategies for Vanadium-based Aqueous Zinc-Ion Batteries, Angew Chem. Int. Edit. 58 (2019) 16358–16367.
[4] G. Zampardi, F.La Mantia, Open challenges and good experimental practices in the research field of aqueous Zn-ion batteries, Nat. Commun. 13 (2022) 687.
[5] Q. Zhang, J. Luan, Y. Tang, X. Ji, H. Wang, Interfacial Design of Dendrite-Free Zinc Anodes for Aqueous Zinc-Ion Batteries, Angew Chem. Int. Edit. 59 (2020) 13180–13191.
[6] D. Kundu, B.D. Adams, V. Duffort, S.H. Vajargah, L.F. Nazar, A high-capacity and long-life aqueous rechargeable zinc battery using a metal oxide intercalation cathode, Nat. Energy 1 (2016).
[7] Y. Lu, H. Zhang, H. Liu, Z. Nie, F. Xu, Y. Zhao, J. Zhu, W. Huang, Electrolyte Dynamics Engineering for Flexible Fiber-Shaped Aqueous Zinc-Ion Battery with Ultralong Stability, Nano Lett 21 (2021) 9651–9660.

[8] P. Xiao, H. Li, J. Fu, C. Zeng, Y. Zhao, T. Zhai, H. Li, An anticorrosive zinc metal anode with ultra-long cycle life over one year, Energ, Environ. Sci. 15 (2022) 1638–1646.
[9] F. Wang, L.E. Blanc, Q. Li, A. Faraone, X. Ji, H.H. Chen-Mayer, R.L. Paul, J.A. Dura, E. Hu, K. Xu, L.F. Nazar, C. Wang, Quantifying and Suppressing Proton Intercalation to Enable High-Voltage Zn-Ion Batteries, Adv. Energy Mater. 11 (2021), 2102016.
[10] C. Zeng, J. Liang, C. Cui, T. Zhai, H. Li, Dynamic investigation of battery materials via advanced visualization: from particle, electrode to cell level, Adv. Mater. (2022), e2200777.
[11] J. Ding, H. Zheng, H. Gao, Q. Liu, Z. Hu, L. Han, S. Wang, S. Wu, S. Fang, S. Chou, In Situ Lattice Tunnel Distortion of Vanadium Trioxide for Enhancing Zinc Ion Storage, Adv. Energy Mater. 11 (2021), 2100973.
[12] L. Xing, K.A. Owusu, X. Liu, J. Meng, K. Wang, Q. An, L. Mai, Insights into the storage mechanism of VS_4 nanowire clusters in aluminum-ion battery, Nano Energy 79 (2021), 105384.
[13] S. Deng, Z. Yuan, Z. Tie, C. Wang, L. Song, Z. Niu, Electrochemically Induced Metal-Organic-Framework-Derived Amorphous V_2O_5 for Superior Rate Aqueous Zinc-Ion Batteries, Angew Chem. Int. Edit. 59 (2020) 22002–22006.
[14] C. Xia, J. Guo, Y. Lei, H. Liang, C. Zhao, H.N. Alshareef, Rechargeable Aqueous Zinc-Ion Battery Based on Porous Framework Zinc Pyrovanadate Intercalation Cathode, Adv. Mater. 30 (2018).
[15] C. Liu, W. Xu, C. Mei, M. Li, W. Chen, S. Hong, W.Y. Kim, S.y. Lee, Q. Wu, A Chemically Self-Charging Flexible Solid-State Zinc-Ion Battery Based on VO_2 Cathode and Polyacrylamide-Chitin Nanofiber Hydrogel Electrolyte, Adv. Energy Mater. 11 (2021), 2003902.
[16] Y. Li, Z. Huang, P.K. Kalambate, Y. Zhong, Z. Huang, M. Xie, Y. Shen, Y. Huang, V_2O_5 nanopaper as a cathode material with high capacity and long cycle life for rechargeable aqueous zinc-ion battery, Nano Energy 60 (2019) 752–759.
[17] M. Yan, P. He, Y. Chen, S. Wang, Q. Wei, K. Zhao, X. Xu, Q. An, Y. Shuang, Y. Shao, K.T. Mueller, L. Mai, J. Liu, J. Yang, Water-Lubricated Intercalation in $V_2O_5{\cdot}nH_2O$ for High-Capacity and High-Rate Aqueous Rechargeable Zinc Batteries, Adv. Mater. 30 (2018).
[18] Z. Wu, C. Lu, F. Ye, L. Zhang, L. Jiang, Q. Liu, H. Dong, Z. Sun, L. Hu, Bilayered $VOPO_4{\cdot}2H_2O$ Nanosheets with High-Concentration Oxygen Vacancies for High-Performance Aqueous Zinc-Ion Batteries, Adv. Funct. Mater. 31 (2021), 2106816.
[19] C. Xia, J. Guo, P. Li, X. Zhang, H.N. Alshareef, Highly Stable Aqueous Zinc-Ion Storage Using a Layered Calcium Vanadium Oxide Bronze Cathode, Angew Chem. Int. Edit. 57 (2018) 3943–3948.
[20] B. Tang, G. Fang, J. Zhou, L. Wang, Y. Lei, C. Wang, T. Lin, Y. Tang, S. Liang, Potassium vanadates with stable structure and fast ion diffusion channel as cathode for rechargeable aqueous zinc-ion batteries, Nano Energy 51 (2018) 579–587.
[21] H. Jiang, Y. Zhang, L. Xu, Z. Gao, J. Zheng, Q. Wang, C. Meng, J. Wang, Fabrication of $(NH_4)_2V_3O_8$ nanoparticles encapsulated in amorphous carbon for high capacity electrodes in aqueous zinc ion batteries, Chem. Eng. J. 382 (2020), 122844.
[22] F. Cui, D. Wang, F. Hu, X. Yu, C. Guan, G. Song, F. Xu, K. Zhu, Deficiency and surface engineering boosting electronic and ionic kinetics in $NH_4V_4O_{10}$ for high-performance aqueous zinc-ion battery, Energy Storage Mater 44 (2022) 197–205.
[23] T. Chen, X. Zhu, X. Chen, Q. Zhang, Y. Li, W. Peng, F. Zhang, X. Fan, VS2 nanosheets vertically grown on graphene as high-performance cathodes for aqueous zinc-ion batteries, J. Power Sources 477 (2020), 228652.
[24] J. Meng, Q. He, L. Xu, X. Zhang, F. Liu, X. Wang, Q. Li, X. Xu, G. Zhang, C. Niu, Z. Xiao, Z. Liu, Z. Zhu, Y. Zhao, L. Mai, Identification of Phase Control of Carbon-Confined Nb_2O_5 Nanoparticles toward High-Performance Lithium Storage, Adv. Energy Mater. 9 (2019), 1802695.
[25] L. Mu, C. Feng, H. He, Topological Research on Lattice Energies for Inorganic Compounds, MATCH-Commun. Math. Co. 56 (2006) 97–111.
[26] J.H. Jo, Y.-.K. Sun, S.-.T. Myung, Hollandite-type Al-doped $VO_{1.52}(OH)_{0.77}$ as a zinc ion insertion host material, J. Mater. Chem. A 5 (2017) 8367–8375.
[27] T. Wei, Q. Li, G. Yang, C. Wang, Highly reversible and long-life cycling aqueous zinc-ion battery based on ultrathin $(NH_4)_2V_{10}O_{25}{\cdot}8H_2O$ nanobelts, J. Mater. Chem. A 6 (2018) 20402–20410.
[28] Y. Yang, Y. Tang, G. Fang, L. Shan, J. Guo, W. Zhang, C. Wang, L. Wang, J. Zhou, S. Liang, Li^+ intercalated $V_2O_5{\cdot}nH_2O$ with enlarged layer spacing and fast ion diffusion as an aqueous zinc-ion battery cathode, Energ. Environ. Sci. 11 (2018) 3157–3162.
[29] Y. Yang, Y. Tang, S. Liang, Z. Wu, G. Fang, X. Cao, C. Wang, T. Lin, A. Pan, J. Zhou, Transition metal ion-preintercalated V2O5 as high-performance aqueous zinc-ion battery cathode with broad temperature adaptability, Nano Energy 61 (2019) 617–625.
[30] W. Zhang, S. Liang, G. Fang, Y. Yang, J. Zhou, Ultra-High Mass-Loading Cathode for Aqueous Zinc-Ion Battery Based on Graphene-Wrapped Aluminum Vanadate Nanobelts, Nano-Micro Lett 11 (2019) 69.
[31] L. Xing, G. Zhao, K. Huang, X. Wu, A yolk-shell V_2O_5 structure assembled from ultrathin nanosheets and coralline-shaped carbon as advanced electrodes for a high-performance asymmetric supercapacitor, Dalton T. 47 (2018) 2256–2265.
[32] J. Zheng, C. Liu, M. Tian, X. Jia, E.P. Jahrman, G.T. Seidler, S. Zhang, Y. Liu, Y. Zhang, C. Meng, G. Cao, Fast and reversible zinc ion intercalation in Al-ion modified hydrated vanadate, Nano Energy 70 (2020), 104519.
[33] A. Aminzadeh, H. Sarikhani-fard, Raman spectroscopic study of Ni/Al_2O_3 catalyst, Spectrochim. Acta A 55 (1999) 1421–1425.
[34] Y. Xu, D. Sun, Structure and catalytic activity of MoZnAlO catalyst for degradation of cationic red GTL under room conditions, Chem. Eng. J. 183 (2012) 332–338.
[35] P. Gao, M.A. Reddy, X. Mu, T. Diemant, L. Zhang, Z. Zhao-Karger, V. S. Chakravadhanula, O. Clemens, R.J. Behm, M. Fichtner, VOCl as a Cathode for Rechargeable Chloride Ion Batteries, Angew Chem. Int. Edit. 55 (2016) 4285–4290.
[36] J. Zheng, Y. Zhang, T. Hu, T. Lv, C. Meng, New Strategy for the Morphology-Controlled Synthesis of V_2O_5 Microcrystals with Enhanced Capacitance as Battery-type Supercapacitor Electrodes, Cryst. Growth Des. 18 (2018) 5365–5376.
[37] Q. Pang, C. Sun, Y. Yu, K. Zhao, Z. Zhang, P.M. Voyles, G. Chen, Y. Wei, X. Wang, $H_2V_3O_8$ Nanowire/Graphene Electrodes for Aqueous Rechargeable Zinc Ion Batteries with High Rate Capability and Large Capacity, Adv. Energy Mater. 8 (2018), 1800144.
[38] L. Wang, K.W. Huang, J. Chen, J. Zheng, Ultralong cycle stability of aqueous zinc-ion batteries with zinc vanadium oxide cathodes, Sci. Adv. 5 (2019) eaax4279.
[39] C. Liu, Z. Neale, J. Zheng, X. Jia, J. Huang, M. Yan, M. Tian, M. Wang, J. Yang, G. Cao, Expanded hydrated vanadate for high-performance aqueous zinc-ion batteries, Energ. Environ. Sci. 12 (2019) 2273–2285.
[40] K. Zhu, T. Wu, K. Huang, $NaCa_{0.6}V_6O_{16}{\cdot}3H_2O$ as an Ultra-Stable Cathode for Zn-Ion Batteries: the Roles of Pre-Inserted Dual-Cations and Structural Water in V_3O_8 Layer, Adv. Energy Mater. 9 (2019), 1901968.
[41] T. Brezesinski, J. Wang, S.H. Tolbert, B. Dunn, Ordered mesoporous alpha-MoO_3 with iso-oriented nanocrystalline walls for thin-film pseudocapacitors, Nat. Mater. 9 (2010) 146–151.
[42] W. Zhou, M. Chen, A. Wang, A. Huang, J. Chen, X. Xu, C.-.P. Wong, Optimizing the electrolyte salt of aqueous zinc-ion batteries based on a high-performance calcium vanadate hydrate cathode material, J. Energy Chem. 52 (2021) 377–384.
[43] M. Tian, C. Liu, J. Zheng, X. Jia, E.P. Jahrman, G.T. Seidler, D. Long, M. Atif, M. Alsalhi, G. Cao, Structural engineering of hydrated vanadium oxide cathode by K^+ incorporation for high-capacity and long-cycling aqueous zinc ion batteries, Energy Storage Mater 29 (2020) 9–16.
[44] L. Zhang, L. Chen, X. Zhou, Z. Liu, Towards High-Voltage Aqueous Metal-Ion Batteries Beyond 1.5 V: the Zinc/Zinc Hexacyanoferrate System, Adv. Energy Mater. 5 (2015), 1400930.
[45] Y. Zhang, L. Xu, H. Jiang, Y. Liu, C. Meng, Polyaniline-expanded the interlayer spacing of hydrated vanadium pentoxide by the interface-intercalation for aqueous rechargeable Zn-ion batteries, J Colloid Interf. Sci. 603 (2021) 641–650.
[46] H. Liu, J.G. Wang, H. Sun, Y. Li, J. Yang, C. Wei, F. Kang, Mechanistic investigation of silver vanadate as superior cathode for high rate and durable zinc-ion batteries, J Colloid Interf. Sci. 560 (2020) 659–666.
[47] Q. Zong, W. Du, C. Liu, H. Yang, Q. Zhang, Z. Zhou, M. Atif, M. Alsalhi, G. Cao, Enhanced Reversible Zinc Ion Intercalation in Deficient Ammonium Vanadate for High-Performance Aqueous Zinc-Ion Battery, Nano-Micro Lett 13 (2021) 116.
[48] M. Li, Z. Li, X. Wang, J. Meng, X. Liu, B. Wu, C. Han, L. Mai, Comprehensive understanding of the roles of water molecules in aqueous Zn-ion batteries: from electrolytes to electrode materials, Energy Storage Mater 14 (2021) 3796–3839.
[49] H. Jiang, Z. Wei, L. Ma, Y. Yuan, J.J. Hong, X. Wu, D.P. Leonard, J. Holoubek, J. J. Razink, W.F. Stickle, F. Du, T. Wu, J. Lu, X. Ji, An Aqueous Dual-Ion Battery Cathode of Mn_3O_4 via Reversible Insertion of Nitrate, Angew Chem. Int. Edit. 58 (2019) 5286–5291.
[50] N. Das, H. Eckert, H. Hu, I.E. Wachs, J.F. Walzer, F.J. Feher, Bonding states of surface vanadium(V) oxide phases on silica: structural characterization by vanadium-51 NMR and Raman spectroscopy, J. Phys. Chem. 97 (2002) 8240–8243.
[51] Q. Li, L. Li, P. Wu, N. Xu, L. Wang, M. Li, A. Dai, K. Amine, L. Mai, J. Lu, Silica Restricting the Sulfur Volatilization of Nickel Sulfide for High-Performance Lithium-Ion Batteries, Adv. Energy Mater. 9 (2019), 1901153.
[52] E. Deiss, Spurious chemical diffusion coefficients of Li^+ in electrode materials evaluated with GITT, Electrochim. Acta 50 (2005) 2927–2932.